Journal of Solid State Chemistry 181 (2008) 3200–3210

Contents lists available at ScienceDirect

Journal of Solid State Chemistry

journal homepage: www.elsevier.com/locate/jssc

Crystal and electronic structures, luminescence properties of Eu^{2+}-doped $Si_{6-z}Al_zO_zN_{8-z}$ and $M_ySi_{6-z}Al_{z-y}O_{z+y}N_{8-z-y}$ (M = 2Li, Mg, Ca, Sr, Ba)

Y.Q. Li *, N. Hirosaki, R.J. Xie, T. Takeda, M. Mitomo

Nitride Particle Group, Nano Ceramics Center, National Institute for Materials Science, Namiki 1-1, Tsukuba, Ibaraki 305-0044, Japan

ARTICLE INFO

Article history:
Received 26 June 2008
Received in revised form
6 August 2008
Accepted 9 August 2008
Available online 19 August 2008

Keywords:
Europium–aluminum–silicon–oxynitride
Lithium and alkaline-earth metal
Crystal structure
X-ray powder diffraction
Luminescence
Electronic structure
DV-Xα

ABSTRACT

The crystal structure, electronic structure, and photoluminescence properties of $Eu_xSi_{6-z}Al_{z-x}O_{z+x}N_{8-z-x}$ (x = 0–0.1, $0<z<1$) and $Eu_xM_ySi_{6-z}Al_{z-x-y}O_{z+x+y}N_{8-z-x-y}$ (M = 2Li, Mg, Ca, Sr, Ba) have been studied. Single-phase $Eu_xSi_{6-z}Al_{z-x}O_{z+x}N_{8-z-x}$ can be obtained in very narrow ranges of $x \leqslant 0.06$ (z = 0.15) and $z<0.5$ (x = 0.3), indicating that limited Eu^{2+} ions can be incorporated into nitrogen-rich $Si_{6-z}Al_zO_zN_{8-z}$. The Eu^{2+} ion is found to occupy the 2*b* site in a hexagonal unit cell ($P6_3/m$) and directly connected by six adjacent nitrogen/oxygen atoms ranging 2.4850–2.5089 Å. The calculated host band gaps by the relativistic DV-Xα method are about 5.55 and 5.45 eV (without Eu^{2+} 4*f*5*d* levels) for x = 0 and 0.013 in $Eu_xSi_{6-z}Al_{z-x}O_{z+x}N_{8-z-x}$ (z = 0.15), in which the top of the 5*d* orbitals overlap with the Si-3*s*3*p* and N-2*p* orbitals within the bottom of the conduction band of the host. $Eu_xSi_{6-z}Al_{z-x}O_{z+x}N_{8-z-x}$ shows a strong green emission with a broad Eu^{2+} band centered at about 530 nm under UV to near-UV excitation range. The excitation and emission spectra are hardly modified by Eu concentration and dual-doping ions of Li and other alkaline-earth ions with Eu. Higher Eu concentrations can significantly quench the luminescence of Eu^{2+} and decrease the thermal quenching temperature. In addition, the emission spectrum can only be slightly tuned to the longer wavelengths (~529–545 nm) by increasing z within the solid solution range of $z<0.5$. Furthermore, the luminescence intensity of $Eu_xSi_{6-z}Al_{z-x}O_{z+x}N_{8-z-x}$ can be improved by increasing z and the dual-doping of Li and Ba.

1. Introduction

Recently, rare-earth-doped Sialon materials have been found to be a new kind of luminescent material, particularly for white-LEDs applications [1–7]. Among two kinds of Sialon materials, i.e. *M*-α-Sialon (M = Ca, Y, Li) and β-Sialon [8–12], *M*-α-Sialon:Eu^{2+} (M = Ca, Y, Li), in particular Ca-α-Sialon:Eu^{2+}, has been extensively investigated and has already been successfully used as a wavelength conversion phosphor in warm-white LEDs [13,14] due to its high absorption in the range 400–460 nm, high quantum efficiency ~80%, and excellent thermal stability. In contrast, the studies of rare-earth-doped β-Sialon are very limited due to the fact that, firstly, the solubility of rare-earth and alkaline-earth ions is significantly low in the host lattice of $Si_{6-z}Al_zO_zN_{8-z}$ and, secondly, there is no appropriate crystallographic site for the bigger cations (i.e. Eu^{2+}) [8–11]. In an earlier work [15], rare earth (Eu, Ce, and Tb) and other ions, like Mn, Ag, activated β-Sialon, have been designed for the purpose of luminescent screen excited by UV, electrons, and X-ray radiation with a focus on the high z range (e.g., z = 3). Thus, β-Sialon:Eu^{2+}, for example, gives the blue emission at about 410–440 nm. More recently, Hirosaki et al. [16] found that Eu^{2+}-doped nitrogen-rich β-Sialon, with a general composition of $Eu_{0.00296}Si_{0.41395}Al_{0.01334}O_{0.0044}N_{0.56528}$, can also be efficiently excited over a broad spectral range between 280 and 480 nm. A green emission band centered at about 535 nm with a full-width at half-maximum (FWHM) of 55 nm is observed. The internal and external quantum efficiencies are about 70% and 61%, respectively, at the excitation wavelength of 303 nm, showing great promise as a green-emitting phosphor for white-light UV-LEDs. Furthermore, by blending green β-Sialon:Eu^{2+} with red ($CaAlSiN_3$:Eu^{2+} [17,18]) and yellow (Ca-α-Sialon:Eu^{2+}) phosphors, white-LED lamps have been generated with higher CRI above 80, covering a broader spectral range [14,19]. Alternatively, β-Sialon:Eu^{2+} phosphor also has been used by combining red $CaAlSiN_3$:Eu^{2+}, yellow Ca-α-Sialon:Eu^{2+} together with a blue-emitting Ce^{3+}-doped JEM phosphor ($La_{1-x}Ce_x(Si_{6-z}Al_z)N_{10-z}O_z$) to generate naturally white light by an UV-LEDs. The obtained CRI is greater than 96 [19]. Most recently, Xie et al. [20] further studied the influence of chemical composition, e.g., Eu concentration and z, on the phase formation, morphology of the particles, and photoluminescence properties as well as on temperature dependence. Moreover, green-emitting β-Sialon:Eu^{2+} exhibits very limited thermal quenching in the temperature range 25–250 °C.

* Corresponding author.
E-mail address: Li.Yuanqiang@nims.go.jp (Y.Q. Li).

0022-4596/$ - see front matter © 2008 Elsevier Inc. All rights reserved.
doi:10.1016/j.jssc.2008.08.012

In the present study, we focus on the investigation of the relationships between the crystal structure and electronic structure on the luminescence of $Eu_xSi_{6-z}Al_{z-x}O_{z+x}N_{8-z-x}$. Here, the general composition of $Eu_xSi_{6-z}Al_{z-x}O_{z+x}N_{8-z-x}$ ($x = 0$–0.1, $0<z\leqslant 1$) is supposedly derived from undoped $Si_{6-z}Al_zO_zN_{8-z}$ by an equivalent cross-substitution of (EuO) for the (AlN) pair. The effects of the Eu content (i.e. x), the composition of the host lattice (i.e. z, with a focus of low z values) and dual-doping with other alkali and alkaline-earth ions on structural and luminescent properties as well as the thermal quenching of $Eu_xSi_{6-z}Al_{z-x}O_{z+x}N_{8-z-x}$ have been studied. Furthermore, the electronic structure calculations have been carried out by the first-principles molecular orbital (MO) method to evaluate the density of states (DOS) in $Eu_xSi_{6-z}Al_{z-x}O_{z+x}N_{8-z-x}$ and gain a deep insight into its luminescence properties.

2. Experimental and computational procedures

2.1. Synthesis

$Eu_xSi_{6-z}Al_{z-x}O_{z+x}N_{8-z-x}$ and $Eu_xM_ySi_{6-z}Al_{z-x-y}O_{z+x+y}N_{8-z-x-y}$ ($M = 2$Li, Mg, Ca, Sr, Ba) were prepared starting from Si_3N_4 (UBE, SN-E10, α content ~93%), AlN (Tokuyama Chemical Co., Ltd., F-grade), Al_2O_3 (Sumitomo Chemical Co., Ltd., AKP-30), Eu_2O_3 (Shin-Etsu Chemical Co., Ltd., purity >99.99%), Li_2CO_3 (High-Purity Chemical Co. Ltd., purity 99.99%), MgO (Konoshima Chemical Co., Ltd., purity >99.9%), $CaCO_3$ (High-Purity Chemical Co. Ltd., purity 99.99%), and MCO_3 (M = Sr, Ba, Aldrich, purity 99%) powders. According to the composition of $Eu_xSi_{6-z}Al_{z-x}O_{z+x}N_{8-z-x}$ ($x = 0$–0.1, $0<z\leqslant 1$) and $Eu_xM_ySi_{6-z}Al_{z-x-y}O_{z+x+y}N_{8-z-x-y}$, the appropriate amount of Si_3N_4, AlN, Al_2O_3, Eu_2O_3, MgO, alkali, and alkaline-earth carbonate powders was homogeneously mixed in a silicon nitride mortar, and the powder mixture was transferred into BN crucibles and then heated at 1900–2000 °C for 4–8 h under a nitrogen atmosphere with a pressure of 0.98 MPa in a gas pressure sintering furnace. The samples were fired twice at the same condition with intermediate grounding in between. The final powders were gently ground for X-ray diffraction and optical measurements.

2.2. Characterizations

The phase formation of the final products was analyzed by X-ray powder diffraction (XRD) (Rigaku, RINT Ultima-III) with a graphite monochromator using Cu-$K\alpha$ radiation ($\lambda = 1.54056$ Å), operating at 40 kV and 40 mA. With regard to structure refinement, the XRD data were collected in the range 10–120° in 2θ by a step-scan mode with a step size of 0.02 and a count time of 10 s per step. The Rietveld refinement was performed by the GSAS package [21,22]. As $Eu_xSi_{6-z}Al_{z-x}O_{z+x}N_{8-z-x}$ and $Eu_xM_ySi_{6-z}Al_{z-x-y}O_{z+x+y}N_{8-z-x-y}$ ($M = 2$Li, Mg, Ca, Sr, Ba) materials are nitrogen-rich with small x and z, the crystal structure of β-Si_3N_4 [23] was used as an initial model for crystal structure refinement. For β-Si_3N_4, both the space groups of $P6_3/m$ and $P6_3$ have been used in the course of the refinement. As those two space groups yielded very similar results, only the refinement with the space group of $P6_3/m$ is given in the present work.

The luminescence spectra were measured by a fluorescence spectrophotometer (Hitachi, F-4500) with a 150 W Xenon short arc lamp as a light source at room temperature. The diffuse reflection spectrum was conducted by a UV–vis spectrophotometer (JASCO, V-560) using a $BaSO_4$ white plate as a standard reference. The quantum efficiency (internal and external quantum efficiency) was recorded on a 200 W Xe-lamp as an excitation source and a Hamamatsu MPCD-7000 multichannel photo detector by a continuous scan model from excitation wavelength 300 to 600 nm with white $BaSO_4$ powder for correction of the absorption. The temperature-dependent luminescence measurement was also carried out by the MCPD-7000 machine under an excitation wavelength of 305 nm from room temperature to 300 °C, holding 5 min for each temperature point.

2.3. Computational method

Using the relativistic DV-Xα code [24–27], first-principles MO calculations were performed on the electronic structure of

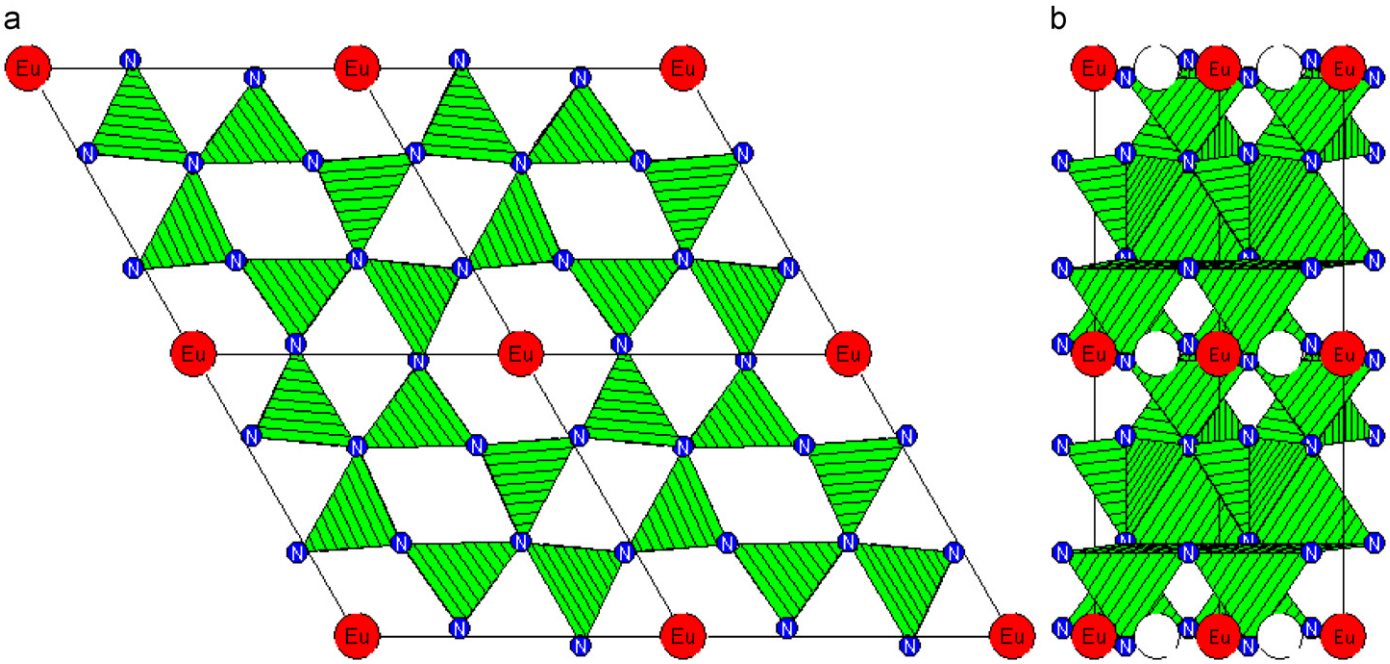

Fig. 1. Crystal structure of $Eu_xSi_{6-z}Al_{z-x}O_{z+x}N_{8-z-x}$, viewed along (a) (001) and (b) (100). The dashed open balls represent the vacancy site of Eu^{2+}.

Table 1
Crystal structure data and the MAPLE value for $Eu_xSi_{6-z}Al_{z-x}O_{z+x}N_{8-z-x}$ ($z = 0.15$, $x = 0$ and 0.013)

Formula		$Si_{6-z}Al_zO_zN_{8-z}$ ($z = 0.15$)					$Eu_xSi_{6-z}Al_{z-x}O_{z+x}N_{8-z-x}$ ($z = 0.15$, $x = 0.013$)				
Crystal system		Hexagonal					Hexagonal				
Space group		$P6_3/m$ (176)					$P6_3/m$ (176)				
Z		2					2				
a (Å)		7.6056(1)					7.6071(1)				
c (Å)		2.9100(1)					2.9097(1)				
V (Å^3)		145.78(1)					145.82(1)				
R_{wp}		13.3%					12.8%				
R_p		9.2%					8.8%				
χ^2		3.8					3.4				
Atom	Wyck	x/a	y/b	z/c	S.O.F.	U (100 Å^2)	x/a	y/b	z/c	S.O.F.	U (100 Å^2)
Si1	6h	0.1741(1)	−0.2309(1)	0.2500	0.9750	0.36	0.1744(1)	−0.2311(1)	0.2500	0.9750	0.33
Al1	6h	0.1741(1)	−0.2309(1)	0.2500	0.0250	0.36	0.1744(1)	−0.2311(1)	0.2500	0.0229	0.33
N1	6h	0.3272(1)	0.0319(1)	0.2500	0.9812	0.15	0.3279(1)	0.0311(1)	0.2500	0.9796	0.11
O1	6h	0.3272(1)	0.0319(1)	0.2500	0.0188	0.15	0.3279(1)	0.0311(1)	0.2500	0.0204	0.11
N2	2c	0.3333	0.6667	0.2500	0.9812	0.63	0.3333	0.6667	0.2500	0.9796	0.53
O2	2c	0.3333	0.6667	0.2500	0.0188	0.63	0.3333	0.6667	0.2500	0.0204	0.53
Eu1	2b	–	–	–	–	–	0.0000	0.0000	0.0000	0.0067	1.90
MAPLE (kJ/mol)		105,183.61					105,134.86				
Sum of the binaries		105,226.74 ($1.925Si_3N_4$+0.15AlN+$0.075SiO_2$)					105,134.94 (0.013EuO+$1.925Si_3N_4$+0.137AlN+$0.075SiO_2$)				
Difference		0.04%					−0.00008%				

$Eu_xSi_{6-z}Al_{z-x}O_{z+x}N_{8-z-x}$ ($x = 0$, 0.013 for $z = 0.15$). Similar to the previous work [28,29], the selected cluster models are extracted from the refined structures, viz $[Si_{12}N_{30}]^{-42}$ and $[EuSi_{12}N_{30}]^{-40}$, respectively, for $x = 0$ and 0.013. The point groups of both clusters have *Ci* symmetry. For the sake of simplicity, a small amount of Al and O was not included in the selected clusters and the relaxation of atoms did not perform in the calculations. The atomic orbitals are based on 1*s*–2*p*, 1*s*–3*p*, and 1*s*–6*p* orbitals for Si, N, and Eu, respectively. In addition, the Madelung potential generated by point charges outside the cluster was introduced into the calculations and the top of the valence band was set at zero energy.

3. Results and discussion

3.1. Structural characteristics

As a solid solution of β-Si_3N_4, $Eu_xSi_{6-z}Al_{z-x}O_{z+x}N_{8-z-x}$ also crystallizes in a centero-symmetric hexagonal system with the space group $P6_3/m$ (or $P6_3$) having an enlarged unit cell owing to the replacement of Si–N by Al–O [8–12]. Within $P6_3/m$, (Si/Al) occupies a 6*h* and two different N occupy 6*h* and 2*c* sites, respectively, in which the corner-connected tetrahedral $(Si/Al)N_4$ build up the framework with a four-ring channel along (001) in the unit cell. Since the smallest radius of this channel is estimated to be about 1.586 Å based on the crystallographic data [23,30,31], it is definitely believed that the Eu^{2+} ion cannot enter such a small channel due to the fact that the Eu–(N/O) bond length is normally above 2.5 Å [32–34] for Eu^{2+}. In the present study, Eu^{2+} was presumably placed in the most promising site in β-S_3N_4 at 2*b* (0,0,0), where the six-ring $(Si/Al)N_4$ tetrahedra constructs a big channel within a $2 \times 2 \times 2$ supercell (Fig. 1a). In addition, considering the interatomic distance of Eu–Eu, if the Eu ions occupy the 2*b* site Eu must be either at (0,0,0) or at (0,0,0.5) but not both in order to lie in the reasonable Eu–Eu distance that is found in many of Eu compounds (the nearest Eu^{2+}–Eu^{2+} distance >3.4 Å) [32–37] (Fig. 1b). By doing so, the crystal structure was refined by the Rietveld method, yielding the reasonable structure of $Eu_xSi_{6-z}Al_{z-x}O_{z+x}N_{8-z-x}$. The crystallographic data of $Eu_xSi_{6-z}Al_{z-x}O_{z+x}N_{8-z-x}$ ($x = 0$ and 0.013 for $z = 0.15$), as the typical examples, are listed in Table 1. Fig. 2 shows the XRD patterns of the Rietveld refinement $Eu_xSi_{6-z}Al_{z-x}O_{z+x}N_{8-z-x}$ ($x = 0$ and 0.013 for $z = 0.15$). Furthermore, the calculated values of the Madelung Partial Lattice Energy (MAPLE) [38–40] of the obtained structures (Table 1) perfectly match with the sum value of the binary constitution compounds with very small discrepancy, which confirms the validation of our proposed crystal structure. In this model, Eu^{2+} is directly coordinated with six (N/O) atoms with the same bond length of 2.4932(18) Å (Table 2). In addition, similar to *M*-α-Sialon (M = Ca, Li), where the distances between *M*–(N/O) are very short (~2.833 Å), the nearest distances between Eu and (Si/Al) are also as short as ~2.7767(7) Å. In this way, therefore, the effect of the change of the Si/Al ratio on Eu^{2+} is expected to be effective. As a result, the luminescence properties of Eu^{2+} should strongly depend on the ratio of Si/Al too (see Section 3.3). It is worth noting that as the nearest Eu–Eu distance is just about 2.9101(3) Å in $Eu_xSi_{6-z}Al_{z-x}O_{z+x}N_{8-z-x}$ ($x = 0.013$, $z = 0.15$), which is much shorter than in that of regular Eu^{2+} compounds as mentioned above [32–37], this could be one of the reasons for very narrow single-phase range of $Eu_xSi_{6-z}Al_{z-x}O_{z+x}N_{8-z-x}$.

3.2. Eu^{2+} concentration, x

Fig. 3 shows the relationship between the lattice parameters and the *x* value of $Eu_xSi_{6-z}Al_{z-x}O_{z+x}N_{8-z-x}$ ($z = 0.15$). In general,

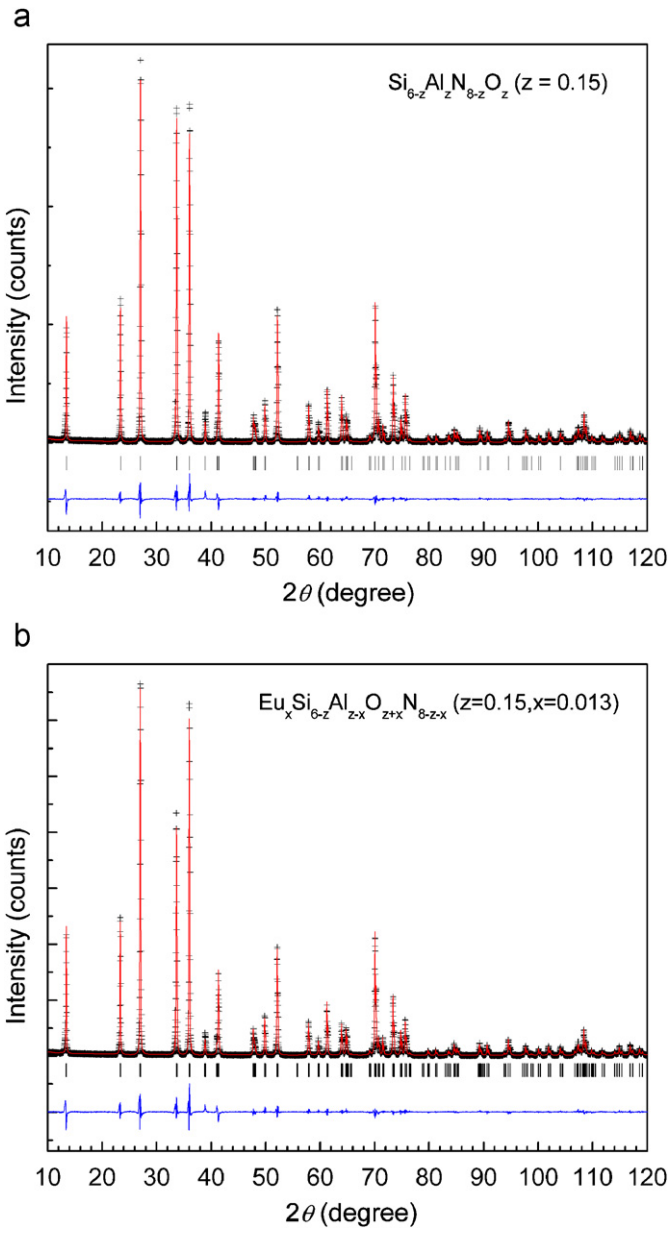

Fig. 2. Observed and calculated Rietveld refinement X-ray powder diffraction patterns of $Eu_xSi_{6-z}Al_{z-x}O_{z+x}N_{8-z-x}$, (a) $x = 0$ and (b) $x = 0.013$ for $z = 0.15$.

Table 2
Selected interatomic distances (Å) and angles (°) for $Eu_xSi_{6-z}Al_{z-x}O_{z+x}N_{8-z-x}$ ($z = 0.15$, $x = 0$ and 0.013)

	$Si_{6-z}Al_zO_zN_{8-z}$ ($z = 0.15$)	$Eu_xSi_{6-z}Al_{z-x}O_{z+x}N_{8-z-x}$ ($z = 0.15$, $x = 0.013$)
(Si/Al)1–(N/O)1	1.7310(11) × 2	1.7348(12) × 2
(Si/Al)1–(N/O)1	1.7387(19)	1.7356(21)
(Si/Al)1–(N/O)2	1.7369(8)	1.7340(8)
Eu1–(N/O)1	–	2.4932(18) × 6
(N/O)1–(Si/Al)1–(N/O)1	106.85(10) × 2	107.21(10) × 2
(N/O)1–(Si/Al)1–(N/O)1	114.39(11)	113.99(12)
(N/O)1–(Si/Al)1–(N/O)2	107.40(8)	107.21(10)
(N/O)1–(Si/Al)1–(N/O)2	110.49(8) × 2	110.44(8) × 2
(N/O)1–Eu1–(N/O)1	–	68.142(11) × 6
(N/O)1–Eu1–(N/O)1	–	111.858(11) × 6
(N/O)1–Eu1–(N/O)1	–	179.92 × 2
(N/O)1–Eu1–(N/O)1		179.98

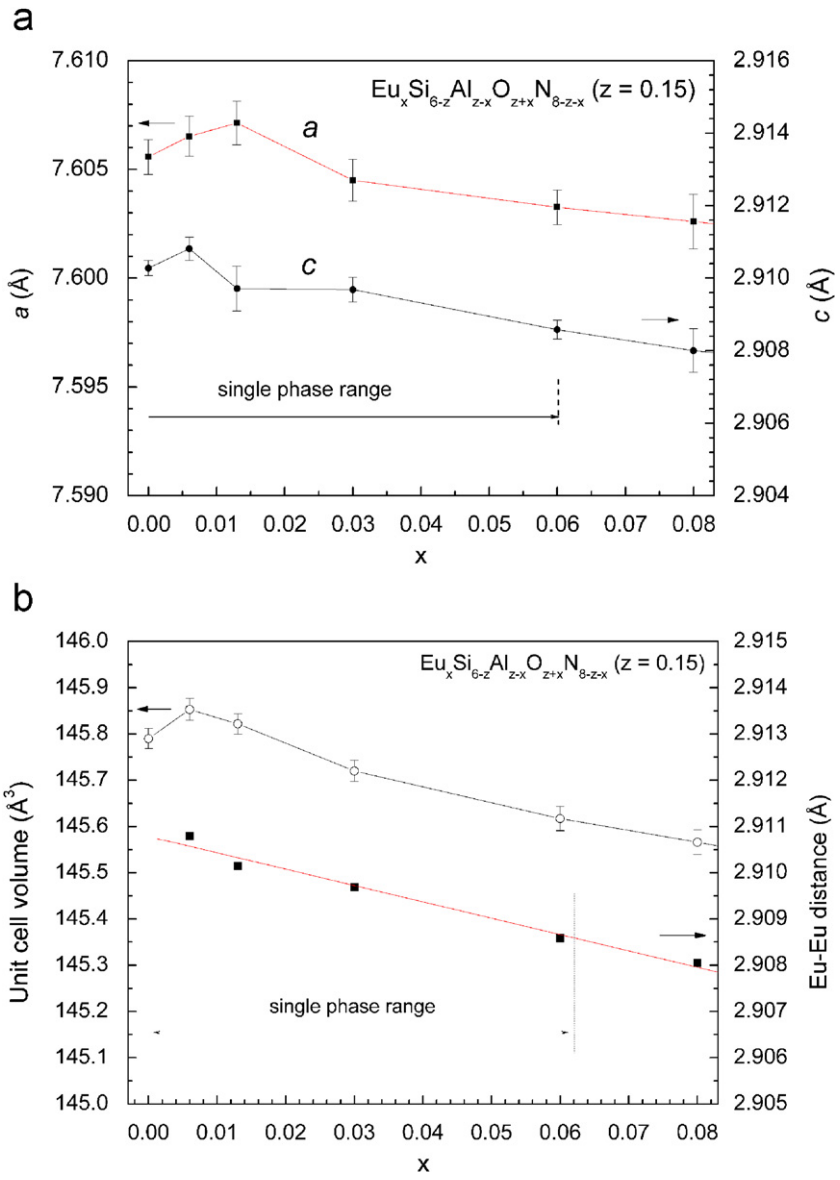

Fig. 3. Lattice parameters and the nearest Eu–Eu distance as a function of x for $Eu_xSi_{6-z}Al_{z-x}O_{z+x}N_{8-z-x}$ ($z = 0.15$).

the introduction of Eu^{2+} into the interstitial site in $Si_{6-z}Al_zO_zN_{8-z}$, the lattice parameters are expected to be increased if the Eu^{2+} ions can be incorporated, although the replacement of nitrogen by oxygen probably somewhat counteracts this effect. Indeed, the lattice parameters clearly show a slight expansion with an increase of x for $z = 0.15$ at low Eu^{2+} concentration ($x < 0.013$) from Fig. 3, which evidently indicates that Eu^{2+} can be incorporated into the $Si_{6-z}Al_zO_zN_{8-z}$ lattice. However, at higher Eu^{2+} concentrations ($x > 0.013$), the lattice parameters show a slight decrease. The contraction of the host lattice is understandable because with increase in x the component of the Al–N pair decreases, which results in framework constricting based on the fact that the Al–(N/O) (~1.75–1.85 Å) bond is longer than that of the Si–(N/O) bond (~1.65–1.74 Å) [8–12,41]. In fact, a very limited volume change (~0.2%) indicates that the overall lattice could be regarded as remaining the same for the incorporation of Eu^{2+}. From the XRD patterns of $Eu_xSi_{6-z}Al_{z-x}O_{z+x}N_{8-z-x}$ ($z = 0.15$) (Fig. 4), the maximum solubility of Eu in $Si_{6-z}Al_zO_zN_{8-z}$ is estimated to be about $x = 0.06$. As a result, when x surpasses 0.06 the second phase is observed, as shown for $x = 0.08$ in Fig. 4.

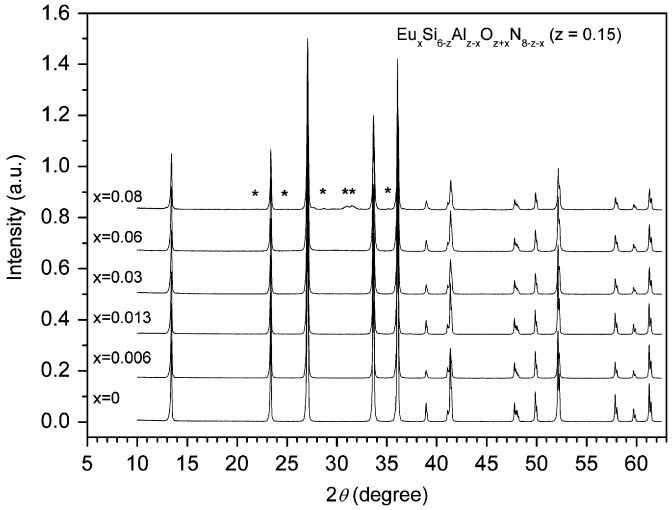

Fig. 4. X-ray powder diffraction patterns of $Eu_xSi_{6-z}Al_{z-x}O_{z+x}N_{8-z-x}$ ($z = 0.15$), * secondary phase.

With a slight change in the lattice parameters, the interatomic distance of Eu–(N/O) shows a slight increase of about 1% in total (2.4850–2.5089 Å). In contrast, the nearest Eu–Eu distance (2.9108–2.9080 Å) shows a linear decrease by about 0.1% (see Fig. 3). Therefore, within the solid solution range, these limited structural variations would be difficult to tune the optical properties just by varying Eu concentration. Another important fact is that the average Eu–(N/O) and Eu–Eu distances in $Eu_xSi_{6-z}Al_{z-x}O_{z+x}N_{8-z-x}$ is much shorter than that in $Eu_2Si_5N_8$ (~2.8161 and 3.418 Å, respectively) [32] and orthorhombic Eu_2SiO_4 (~2.7663 and 3.644 Å, respectively) [33] compounds having the silicon-based lattices. Therefore, the repulsive force between Eu^{2+}–Eu^{2+} and Eu–(N/O), in particular Eu–Eu, would be very strong, which eventually results in the crystal structure being unstable at higher Eu concentrations. In addition, the average bond overlap population value is negative (−0.035), obtained by the DV-Xα MO calculation, which shows strong antibonding characteristics for the nearest Eu–(N/O), in agreement with the experimental observation of a low solubility of Eu in $Si_{6-z}Al_zO_zN_{8-z}$.

3.3. Incorporation of Al–O, z

In contrast to the incorporation of Eu, a single-phase $Eu_xSi_{6-z}Al_{z-x}O_{z+x}N_{8-z-x}$ can only be obtained for $z \leqslant 0.5$ by the incorporation of Al–O. With increasing z the lattice parameters obviously increase up to $z = 1$ (Fig. 5) and a further increase of the lattice parameters is also observed at higher z values as a result of the replacement of Si–N (~1.74 Å) by Al–O (~1.75–1.85 Å) in the framework [8–12,41]. This is confirmed by the Rietveld refinement data, for which the average (Si/Al)–(N/O) bond lengths are about 1.7344(14), 1.7364(12), and 1.7382(18) Å for z of 0.15, 0.3, and 0.5, respectively. For $z \geqslant 0.5$, a small amount of unidentified second phase has been clearly observed from their XRD patterns (their XRD patterns not shown), suggesting a very narrow single-phase range of solid solution in the present synthetic approach and conditions for $Eu_xSi_{6-z}Al_{z-x}O_{z+x}N_{8-z-x}$. In correspondence with the expansion of the host lattice by an increase in z, the nearest distance of Eu–Eu, and the average distances of Eu–(N/O) and (Si/Al)–(N/O) are increased by about 0.56%, 0.72%, and 0.42%, respectively; even in the mixture phase range they still show an

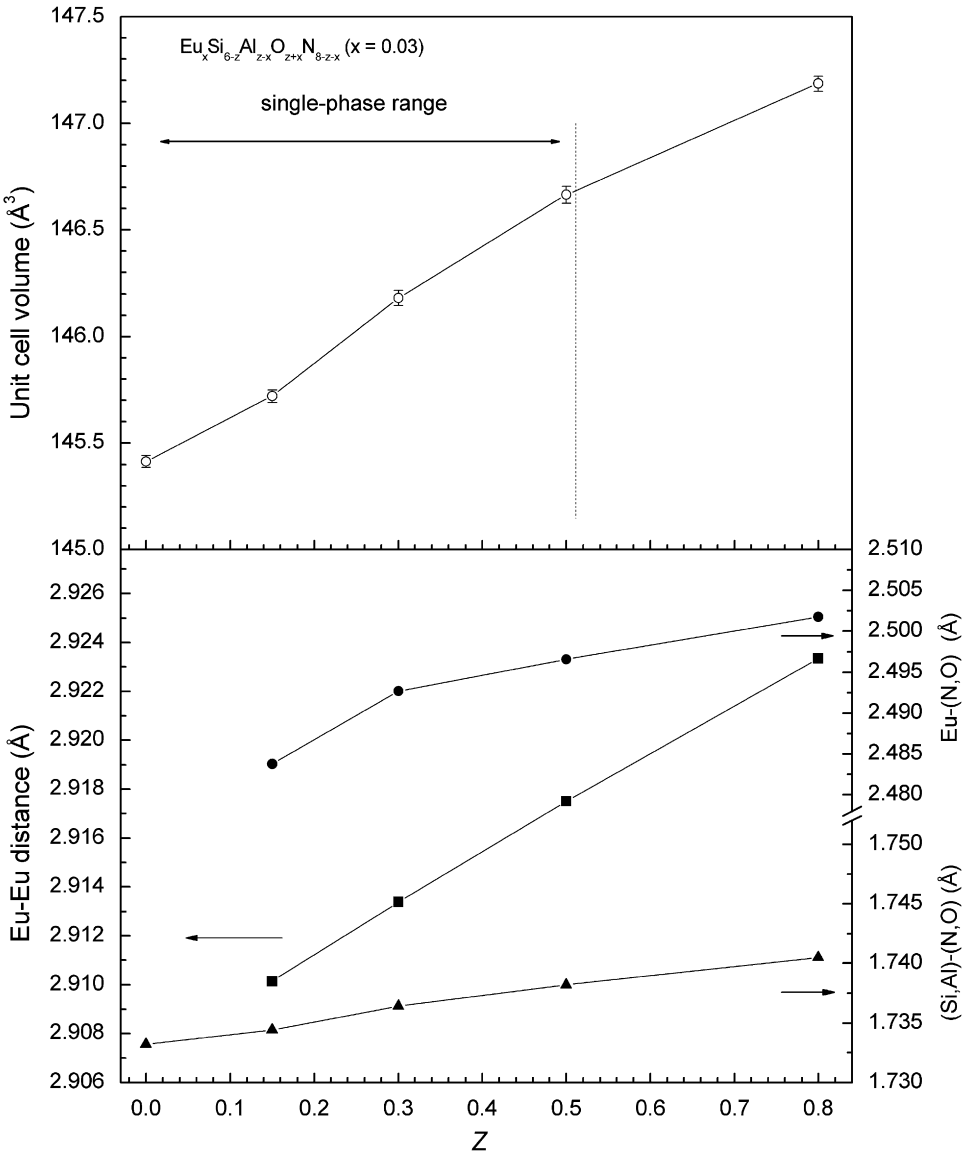

Fig. 5. Lattice parameters and average interatomic distances as a function of z in $Eu_xSi_{6-z}Al_{z-x}O_{z+x}N_{8-z-x}$ ($x = 0.03$).

increased tendency, as shown in Fig. 5. With these structural changes by the incorporation of Al–O, the luminescence properties of $Eu_xSi_{6-z}Al_{z-x}O_{z+x}N_{8-z-x}$ are expected to exhibit a large displacement of the emission spectrum and different quantum efficiency (see Section 3.3).

3.4. Effect of dual-doping M (M = 2Li, Mg, Ca, Sr, Ba)

It is well known that a large amount of Ca, Li, and Mg ions can be easily filled into the interstitial site of the α-Sialon structure in single- or dual-doping ways [8–12] with a solubility sequence of Ca > Li > Mg. According to the type of doping ions, the emission band of Eu^{2+}-doped *M*-α-Sialon (*M* = Ca, Li, Mg) changes from long wavelength for Ca (~580–600 nm) [1–4] to short wavelength for Li (~565–580 nm) [6]. It is also known that the solubility of Li, Ca, Mg, and Sr in β-Sialon is very limited in comparison with α-Sialon [8–12]. Structurally, we want to verify in another way whether or not the Eu^{2+} ion can be really filled into the six-ring tetrahedral channel formed by a $2\times2\times2$ supercell of $Si_{6-z}Al_zO_zN_{8-z}$. If Eu^{2+} can go to the channel, the smaller Li^+, Mg^{2+}, and Ca^{2+} ions might have high solubility and the larger Sr^{2+} and Ba^{2+} might have low solubility in $Si_{6-z}Al_zO_zN_{8-z}$ due to the size effect. Indeed, we found it is real for doping Li^+, Mg^{2+}, Ca^{2+}, Sr^{2+}, and Ba^{2+} in $Si_{6-z}Al_zO_zN_{8-z}$ ($z = 0.03$). Li^+, Mg^{2+}, and Ca^{2+} ions can be incorporated into the host lattice in a large amount; for example, the solubility of Ca^{2+} can reach up to $x = 0.06$–0.08 for $Ca_xSi_{6-z}Al_{z-x}O_{z+x}N_{8-z-x}$ ($z = 0.03$) while the solubility of Eu^{2+} is only about $x = 0.03$ or slightly high for $Eu_xSi_{6-z}Al_{z-x}O_{z+x}N_{8-z-x}$ ($z = 0.03$). This also holds for Li^+ and Mg^{2+} cases. Unfortunately, we could not find a regular change in the lattice parameters with an increase in ionic size in the order of Li < Mg < Ca < Sr < Ba for $Eu_xM_ySi_{6-z}Al_{z-x-y}O_{z+x+y}N_{8-z-x-y}$ ($x = 0$ or 0.013 for $y = 0.017$ and $z = 0.15$, respectively). However, it can be clearly seen from their XRD patterns that the solid solution of $Eu_xM_ySi_{6-z}Al_{z-x-y}O_{z+x+y}N_{8-z-x-y}$ is the ionic size dependence in which *M* = 2Li, Mg, Ca are single-phase solid solutions, while *M* = Sr and Ba are impurity-phase solid solutions with a small amount of unidentified second phase (Fig. 6), implying that the channel along (001) can accommodate a relatively large amount of small ions but not the ions larger than the Sr^{2+} ion. Of course, the doping amounts in $Si_{6-z}Al_zO_zN_{8-z}$ are still much smaller than that in *M*-α-Sialon (*M* = Ca, Mg, and Li) [8–12]; therefore, it may explain a very limited geometric change/relaxation in the $Eu_xM_ySi_{6-z}Al_{z-x-y}O_{z+x+y}N_{8-z-x-y}$ lattice. As a result, the influence of the type of *M* on the luminescence properties would be expected to be small.

3.5. Electronic structure of $Eu_xSi_{6-z}Al_{z-x}O_{z+x}N_{8-z-x}$ (x = 0 and 0.013, z = 0.15)

Similar to *M*-α-Sialon (*M* = Ca) [42] and β-$Si_{6-z}Al_zO_zN_{8-z}$ [43], the optical band gap of $Eu_xSi_{6-z}Al_{z-x}O_{z+x}N_{8-z-x}$ can also be changed by varying the Eu (i.e., *x*) concentration because the change in *x* can also alter the composition of the framework (i.e., (Si,Al)–(N,O)) simultaneously. Experimentally, $Eu_xSi_{6-z}Al_{z-x}O_{z+x}N_{8-z-x}$ cannot be directly used to determine the optical band gap due to strong Eu^{2+} absorption bands in the UV range in the diffuse reflection spectra. Therefore, $Sr_xSi_{6-z}Al_{z-x}O_{z+x}N_{8-z-x}$ ($z = 0.15$, $x = 0.013$–0.05) were used as references for this purpose considering the similar structure features in a large number of Eu and Sr isomorphous compounds [32–36,44,45]. The estimated optical band gaps for $Sr_xSi_{6-z}Al_{z-x}O_{z+x}N_{8-z-x}$ are about 5.57 and 5.44 eV for $x = 0.013$ and 0.03 at $z = 0.15$, respectively, which indirectly supports the above argument that the band gap decreases with a decrease in the amount of Al–N. In particular, $Ca_xSi_{6-z}Al_{z-x}O_{z+x}N_{8-z-x}$ ($z = 0.15$) is more remarkable with the variation of *x*. The fundamental optical absorption edge significantly shifts towards the long wavelength against $Si_{6-z}Al_zO_zN_{8-z}$ ($z = 0.15$) and $Sr_xSi_{6-z}Al_{z-x}O_{z+x}N_{8-z-x}$ ($z = 0.15$, $x = 0.013$) with a decrease in the optical band gap from about 4.85 via 4.81–4.76 eV for $x = 0.02$, 0.04, and 0.06, respectively, as shown in Fig. 7.

Fig. 8 shows the selected cluster models of $Eu_xSi_{6-z}Al_{z-x}O_{z+x}N_{8-z-x}$ ($z = 0.15$, $x = 0$, 0.013) from the Rietveld refined powder XRD data for the DV-Xα calculations. The total and partial DOS of $Eu_xSi_{6-z}Al_{z-x}O_{z+x}N_{8-z-x}$ ($x = 0$ and 0.013 for $z = 0.15$, respectively) are shown in Fig. 9. In good agreement with the experimental data, the calculated band gap between the highest occupied molecular orbital (HOMO) and the lowest unoccupied molecular orbital (LUMO) decreases from ca. 5.55 to 5.45 eV as incorporated Eu^{2+} into the $Si_{6-z}Al_zO_zN_{8-z}$ lattice. It should be noted that an accurate calculation of the band gap is not the main purpose of the present work, and actually it strongly depends on the size of the selected cluster for the DV-Xα method. The conduction band is composed of the Si-3*s* and Si-3*p* as well as small partial N-2*p* orbitals while the Si-3*s* orbital dominates the bottom of the conduction band for $Si_{6-z}Al_zO_zN_{8-z}$ ($z = 0.15$). In the

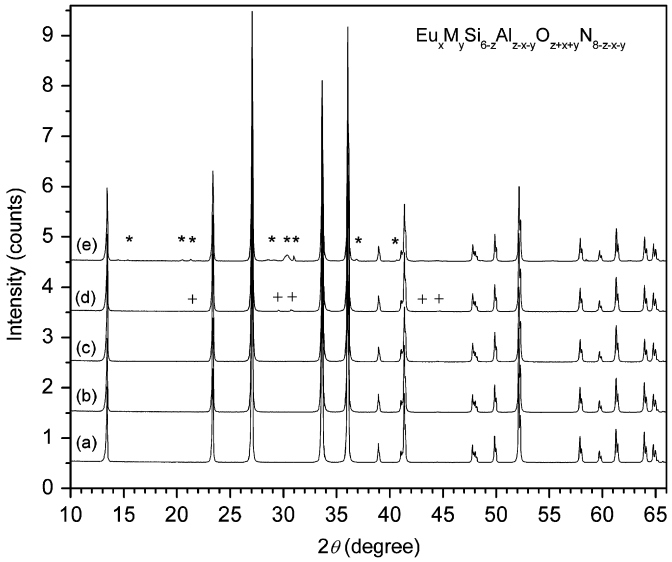

Fig. 6. X-ray powder diffraction patterns of $Eu_xM_ySi_{6-z}Al_{z-x-y}O_{z+x+y}N_{8-z-x-y}$: (a) Li, (b) Mg, (c) Ca, (d) Sr, and (e) Ba ($x = 0.013$, $y = 0.017$, $z = 0.15$).

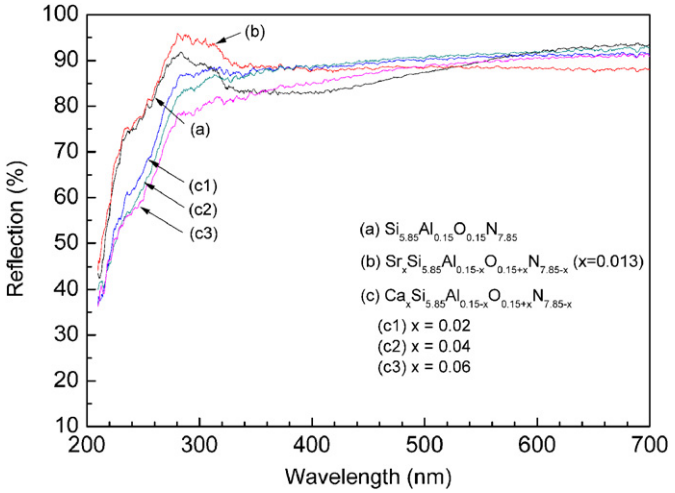

Fig. 7. Diffuse reflection spectra of $Si_{6-z}Al_zO_zN_{8-z}$ ($z = 0.15$) and $M_xSi_{6-z}Al_{z-x}O_{z+x}N_{8-z-x}$ (*M* = Sr, Ca, $z = 0.15$).

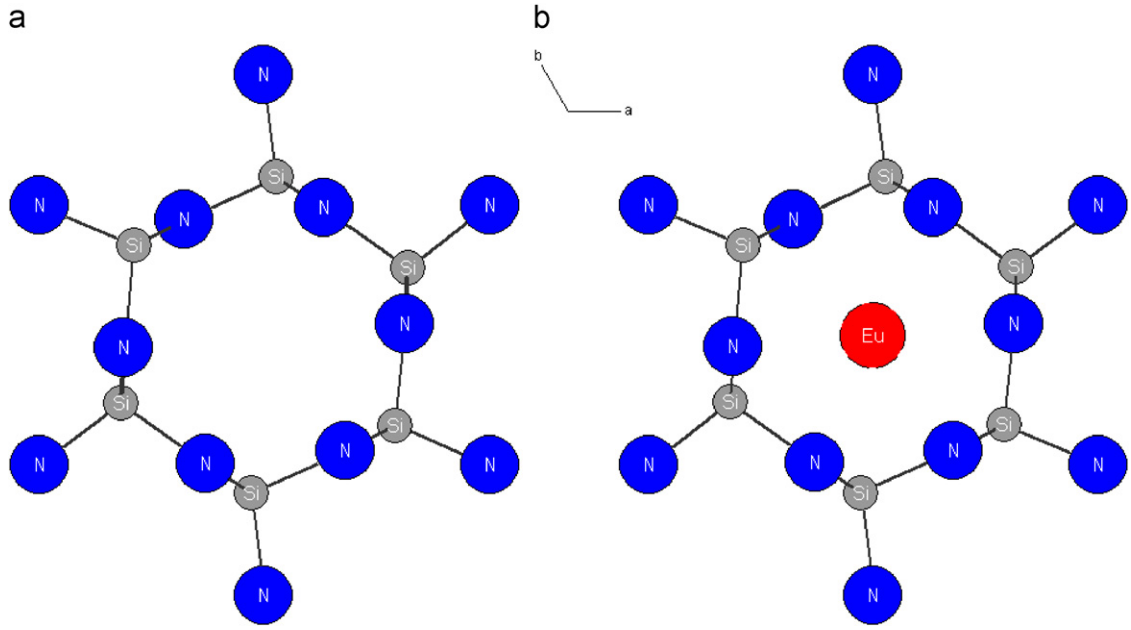

Fig. 8. The cluster models of (a) $[Si_{12}N_{30}]^{-42}$ and (b) $[EuSi_{12}N_{30}]^{-40}$ of $Eu_xSi_{6-z}Al_{z-x}O_{z+x}N_{8-z-x}$ ($z=0.15$) for $x=0$ and 0.013, respectively.

case of $Eu_xSi_{6-z}Al_{z-x}O_{z+x}N_{8-z-x}$ ($x=0.013$, $z=0.15$), partial high levels of the Eu-5*d* orbitals are hybridized with the Si-3*s*, Si-3*p* and N-2*p* orbitals at the bottom of the conduction band (Fig. 9), suggesting that the 5*d* electrons of Eu^{2+} take part in the formation of chemical bonding, which is influenced by its neighbor atoms, in particular the second nearest Si (or Si/Al) atom from the viewpoint of the electronic structure . The valence bands mainly consist of N-2*s*, and N-2*p* hybridized with a small amount of Si-3*s* and Si-3*p* dispersed at lower energies for $Eu_xSi_{6-z}Al_{z-x}O_{z+x}N_{8-z-x}$ ($x=0$, 0.013) with the N-2*s* orbital clearly separating from the other orbitals of the valence bands at much lower energies, whereas the N-2*p* orbitals are at the top of the valence band. The calculated 4*f* and 5*d* levels of Eu^{2+} are located in between the conduction and valence band just below the bottom of the conduction band. In addition, an overlap of the top of the Eu-5*d* orbitals with the Si-3*s*3*p* and N-2*p* orbitals at the bottom of the conduction band is not favorable for luminescent applications, which is probably related to its small crystallographic sites. Nevertheless, we should address the fact that the calculation precisely is not good enough without including Al and O, and the relative position of the 4*f* and 5*d* orbitals of Eu^{2+} is also far from satisfaction only by the DV-Xα method, which should combine with other appropriate first-principles methods to produce the accurate results. In short, the DV-Xα calculations strongly confirm our experimental results from the diffuse reflection spectra, in which the band gap is slightly narrowed by Eu doping in $Si_{6-z}Al_zO_zN_{8-z}$ theoretically. Furthermore, the large hybridization of Eu-5*d* with Si-3*s*3*p* and N-2*p* orbitals indicates that the 5*d* states of Eu^{2+} are more sensitive to Si (or Si/Al) in agreement with the obtained structural data (see Section 3.1).

3.6. Luminescence properties

3.6.1. $Eu_xSi_{6-z}Al_{z-x}O_{z+x}N_{8-z-x}$ ($z=0.15$)

Fig. 10(a) shows the excitation and emission spectra of $Eu_xSi_{6-z}Al_{z-x}O_{z+x}N_{8-z-x}$ ($z=0.15$). The dominant excitation band is a broad band peaking at about 300 nm, and the second strongest excitation band is at about 400 nm with several weak shoulders at longer wavelengths (e.g., ~450 nm). Moreover, when we combine the reflection (Fig. 7) and excitation (Fig. 10) spectra, it is clear that the absorption edge of $M_xSi_{6-z}Al_{z-x}O_{z+x}N_{8-z-x}$ (M = Sr, Eu, Ca, etc.) is located within the main excitation band of Eu^{2+} and is very close to its maximum, in good agreement with the calculated result of DV-Xα. The broad emission band at about 530 nm is attributed to the $4f^65d^1 \rightarrow 4f^7$ transition of Eu^{2+}. It can be found that both the excitation and emission intensity can be increased only in lower Eu concentrations corresponding to the expansion of the $Eu_xSi_{6-z}Al_{z-x}O_{z+x}N_{8-z-x}$ ($z=0.15$, $x<0.013$) lattice (Fig. 3). However, at higher Eu concentrations with the shrinkage of the lattice, both the emission intensity (Fig. 10a) and the external quantum efficiency (Fig. 10b) significantly decrease. Because both the excitation and emission bands are almost fixed and hardly vary with *x*, showing a slight blue shift, the change in the Stokes shift can be neglected in $Eu_xSi_{6-z}Al_{z-x}O_{z+x}N_{8-z-x}$. This unchangeable position of the excitation and emission bands can be well explained by its very low Eu concentration (i.e., low *x*) providing low possibility for energy transfer of Eu^{2+} and by its very limited lattice relaxation. On the other hand, a slight blue shift might be ascribed to an increase in the Si/Al ratio in $Eu_xSi_{6-z}Al_{z-x}O_{z+x}N_{8-z-x}$ with increasing *x*, similar to Ca-α-Sialon: Eu^{2+} [6–9].

As mentioned above, the quantum efficiency increases just in the lattice expansion range ($x<0.013$) and then decreases in the lattice shrinkage region. The photoluminescence intensity and quantum efficiency reach a maximum at about $x=0.013$, i.e., external Q.E. ~54% and 32% for excitation at 300 and 405 nm, respectively. When $x>0.013$, both the luminescence intensity and quantum efficiency show a remarkable decrease with increasing Eu concentration. The most possible reason responsible for quenching of the luminescence is the photoionization process [46] as the top of Eu^{2+} 5*d* excitation states overlap with the bottom of the conduction bands of the host lattice due to band gap narrowing by the introduction of Eu^{2+} as described in Section 3.2, suggesting that the 5*d* electrons can easily be ionized in its excited state from the luminescent center to the conduction band of the host. Subsequently, the promoted electrons would recombine with the holes formed at the Eu^{2+} sites and markedly quench the photoluminescence in the way of nonradiative transitions. The holes formation at the Eu^{2+} site may be indirectly deduced based

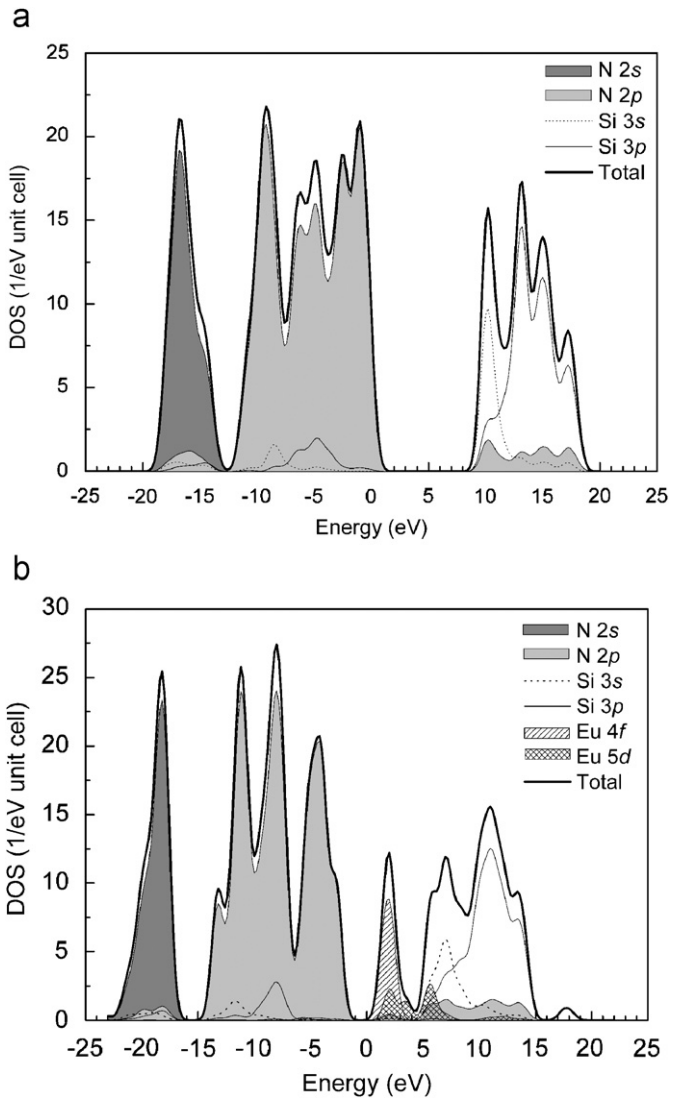

Fig. 9. Total and partial density of states (DOS) of $Eu_xSi_{6-z}Al_{z-x}O_{z+x}N_{8-z-x}$ ($z = 0.15$): (a) $x = 0$ and (b) $x = 0.013$.

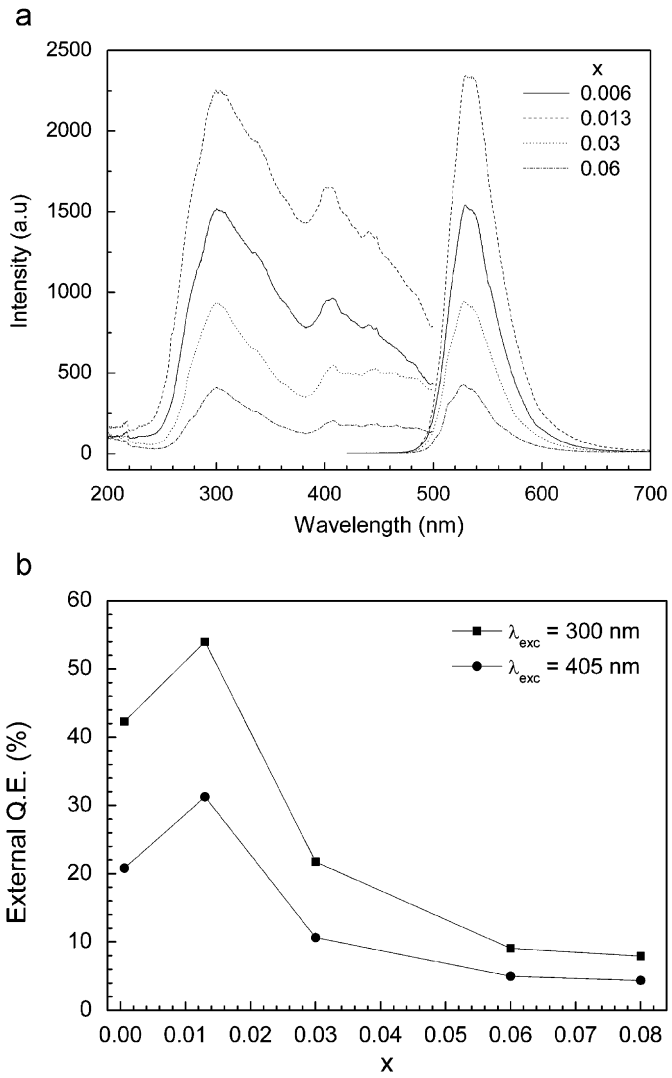

Fig. 10. Excitation and emission spectra (a), and quantum efficiency (b) of $Eu_xSi_{6-z}Al_{z-x}O_{z+x}N_{8-z-x}$ ($z = 0.15$) as a function of x.

on the XRD results. In $M_xSi_{6-z}Al_{z-x}O_{z+x}N_{8-z-x}$ (M = Eu, Sr, $z = 0.15$), the maximum solubility of Eu can reach up to $x = 0.06$ or more (see Figs. 4 and 6), whereas that of Sr^{2+} is less than $x = 0.03$, corresponding to the appearance of the second phase in its XRD pattern when $x \geqslant 0.03$ (XRD patterns not shown). Because of the very similar ionic size of Sr^{2+} (~1.18 Å for C.N. = 6) and Eu^{2+} (~1.17 Å for C.N. = 6), they should also give a similar solubility for the formation of interstitial solid solutions if they have the same charge (i.e., +2). However, a high solubility of Eu^{2+} implies that some Eu^{2+} probably transfer to smaller Eu^{3+} ions (~0.95 Å for C.N. = 6) by losing one electron and leaving one hole at the Eu^{2+} site. In this way, the small [Eu^{2+} (Eu^{3+})] ions can be incorporated into the channel in a large amount. This also supports the fact that their body color changes from blue-green to light white-brown under daylight with an increase in Eu concentration because Eu^{3+} is colorless in the visible spectrum range.

Fig. 11 shows the relative emission intensity as a function of temperature (25–300 °C). The luminescence quenching temperature (T_{50}, the temperature at half of its maximum emission intensity at room temperature) of $Eu_xSi_{6-z}Al_{z-x}O_{z+x}N_{8-z-x}$ is estimated to be above 300 °C and the emission peak of Eu^{2+} just shows a smaller red-shift at high temperatures. The higher Eu concentrations not only quench the luminescence but also result

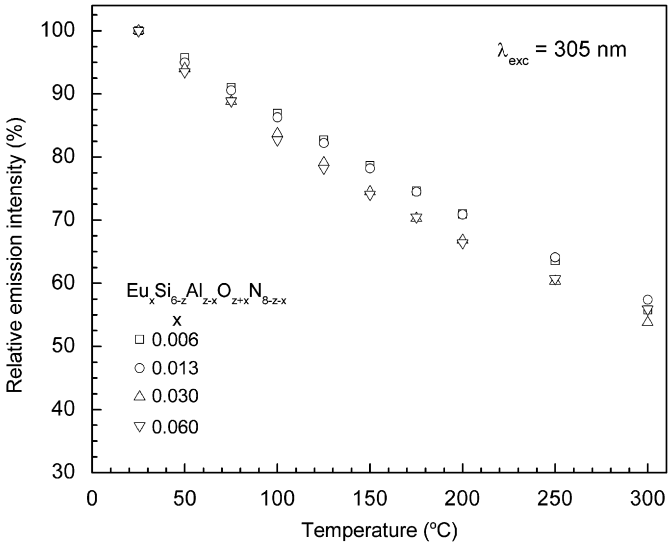

Fig. 11. Temperature dependence of $Eu_xSi_{6-z}Al_{z-x}O_{z+x}N_{8-z-x}$ ($x = 0.006$–0.060, $z = 0.15$) under excitation at 305 nm.

in high thermal quenching rates. Because of a negligible Stokes shift change, the thermal quenching may be mainly related to the thermal ionization process of Eu^{2+} [47,48], which originates from the band gap narrowing of $Eu_xSi_{6-z}Al_{z-x}O_{z+x}N_{8-z-x}$ by temperature [49,50].

3.6.2. $Eu_xSi_{6-z}Al_{z-x}O_{z+x}N_{8-z-x}$ ($x = 0.03$)

Like Ca-α-Sialon:Eu^{2+}, modification of the second nearest atoms around the Eu^{2+} activator is an effective way of manipulating the luminescence behaviors of $Eu_xSi_{6-z}Al_{z-x}O_{z+x}N_{8-z-x}$ as the lattice can be largely relaxed by varying z (see Fig. 5). When the z value increases, although no obvious changes have been observed for the profile of the excitation spectra of $Eu_xSi_{6-z}Al_{z-x}O_{z+x}N_{8-z-x}$ ($x = 0.03$, $z = 0.15$–0.5), the position of the emission band of Eu^{2+} significantly shifts to long wavelengths from about 529 to 545 nm up to $z = 0.5$ (Fig. 12a). Additionally, the intensity of the excitation and emission bands gradually increases with increase in z from 0.15 to 1.0. Correspondingly, the external quantum efficiency shows the same tendency at the excitation wavelength of 300 and 405 nm (see Fig. 12b). The presence of the secondary phase has no marked influences on the quantum efficiency. However, an additional emission shoulder at short wavelength around 480 nm appears when $z \geqslant 0.5$ (see inset in Fig. 12b). Certainly, this emission shoulder for high z is associated with the second phases. Due to an independent relationship between the excitation spectrum and z, the central of gravity (~29,378 cm^{-1}) and the crystal filed splitting (~14,616 cm^{-1}) of the 5d states of Eu^{2+} estimated from the excitation spectrum are almost fixed by the structure/composition. The red-shift of the emission band could be mainly assigned to the Stokes shift arising from the structural expansion, which would result in a large relaxation of the 5d electron of Eu^{2+} in the $5d \rightarrow 4f$ transition due to the replacement of Si–N by Al–O. The enlargement of the nearest Eu–Eu as well as Eu-(Si/Al) distances are responsible for improvement of the quantum efficiency of $Eu_xSi_{6-z}Al_{z-x}O_{z+x}N_{8-z-x}$, as shown in Fig. 12b.

3.6.3. $Eu_xM_ySi_{6-z}Al_{z-x-y}O_{z+x+y}N_{8-z-x-y}$ ($x = 0.013$, $y = 0.017$, $z = 0.15$, $M = 2Li, Mg, Ca, Sr, Ba$)

As shown in Fig. 13a, the excitation and emission spectra are similar to $Eu_xSi_{6-z}Al_{z-x}O_{z+x}N_{8-z-x}$, but dual-doping Li and Ba can increase whereas Mg, Ca, and Sr decrease the photoluminescence intensity in comparison with $Eu_xSi_{6-z}Al_{z-x}O_{z+x}N_{8-z-x}$. In particular, incorporation of Ca remarkably decreases the luminescence intensity varying with the Ca content (Fig. 13b) because of the enhanced photoionization process of the 5d electron of Eu^{2+}, which can be seen clearly from their reflection (Fig. 7)

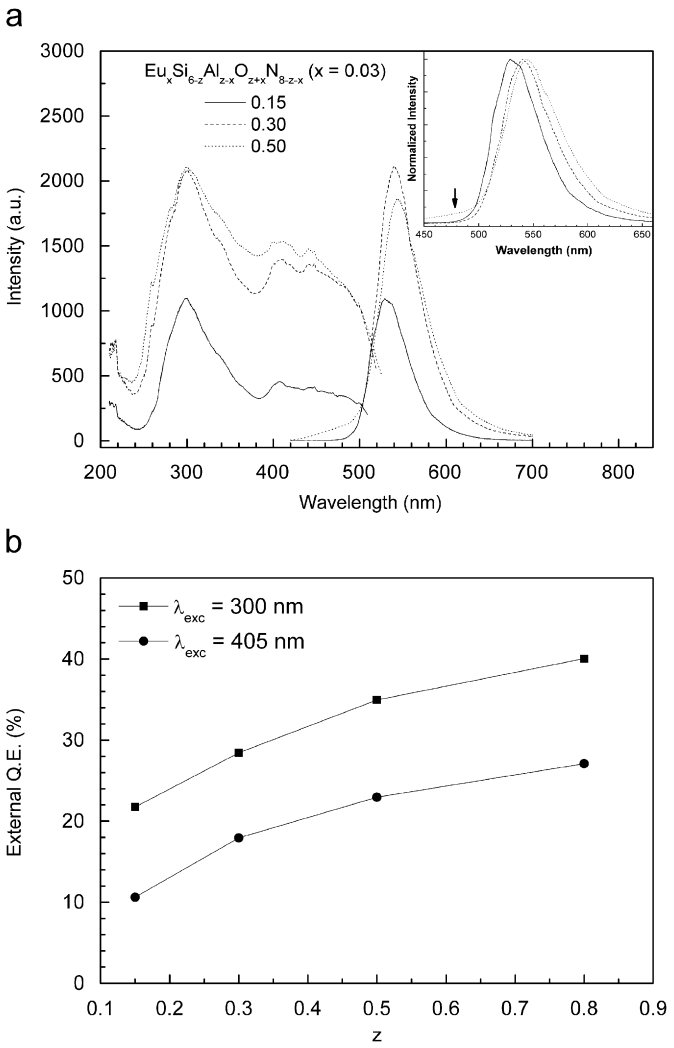

Fig. 12. Excitation and emission spectra (a), and quantum efficiency (b) of $Eu_xSi_{6-z}Al_{z-x}O_{z+x}N_{8-z-x}$ ($x = 0.03$) as a function of z. The arrow in inset indicates an additional emission shoulder of Eu^{2+} for $z = 0.5$.

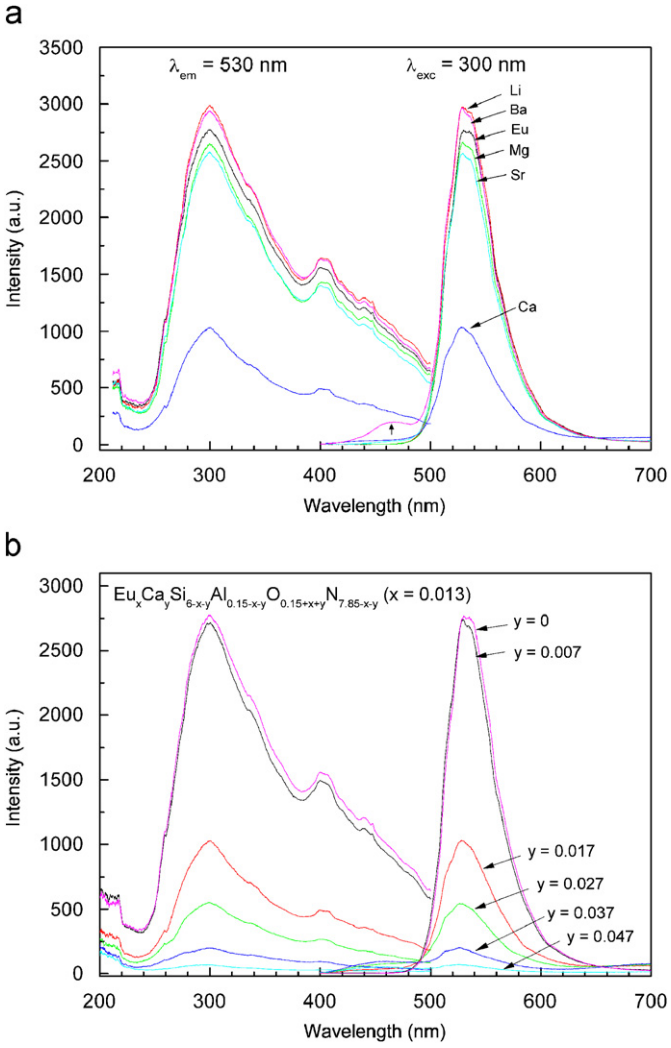

Fig. 13. (a) Excitation and emission spectra of $Eu_xM_ySi_{6-z}Al_{z-x-y}O_{z+x+y}N_{8-z-x-y}$ varying with the type of M (M = 2Li, Mg, Ca, Sr, Ba). (b) Excitation and emission spectra of $Eu_xCa_ySi_{6-x-y}Al_{0.15-x-y}O_{0.15+x+y}N_{7.85-x-y}$ ($x = 0.013$) varying with y.

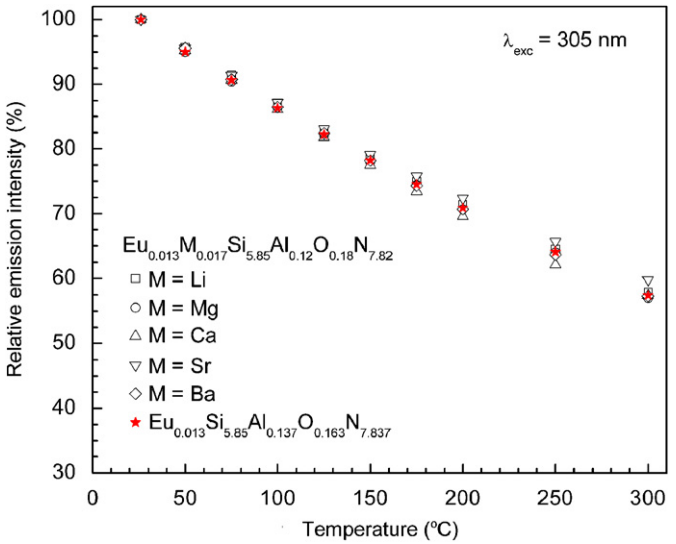

Fig. 14. Temperature dependence of $Eu_xM_ySi_{6-z}Al_{z-x-y}O_{z+x+y}N_{8-z-x-y}$ ($x=0.013$, $z=0.15$) and $Eu_xSi_{6-z}Al_{z-x}O_{z+x}N_{8-z-x}$ ($x=0.013$, $z=0.15$) under excitation at 305 nm.

and excitation (Fig. 13b) spectra, where the fundamental absorption edge of $Ca_xSi_{6-z}Al_{z-x}O_{z+x}N_{8-z-x}$ largely overlaps the main excitation band at about 300 nm in $Eu_xCa_ySi_{6-z}Al_{z-x-y}O_{z+x+y}N_{8-z-x-y}$. In contrast, the luminescence intensity is increased by the dual-doping of Li and Ba, which may be related to a large optical band gap (i.e. Li and Ba do not narrow the band gap of $Si_{6-z}Al_zO_zN_{8-z}$ (Fig. 7)) and an increased degree of crystallization. Additionally, the influence of dual-doping of Eu^{2+}–Li^+ and Eu^{2+}–Ba^{2+} on the thermal quenching behavior is significantly small (Fig. 14), indicating that it is a useful way to improve the luminescence intensity/quantum efficiency of $Eu_xSi_{6-z}Al_{z-x}O_{z+x}N_{8-z-x}$.

4. Conclusions

(1) $Eu_xSi_{6-z}Al_{z-x}O_{z+x}N_{8-z-x}$ is isostructural to $Si_{6-z}Al_zO_zN_{8-z}$ crystallized in a hexagonal system with the space group $P6_3/m$, in which Eu is situated at the 2*b* site (0,0,0) within the channel of six-SiN tetrahedral rings formed by a $2\times2\times2$ supercell of $Si_{6-z}Al_zO_zN_{8-z}$ along (100). The single-phase range of $Eu_xSi_{6-z}Al_{z-x}O_{z+x}N_{8-z-x}$ narrowly exists at about $x\leqslant0.06$ for $z=0.15$ and $z<0.5$ for $x=0.3$.

(2) The relativistic DV-Xα MO cluster calculation indicates that the Eu^{2+}-4*f* and 5*d* as impurity levels are located between the conduction and valence bands of $Si_{6-z}Al_zO_zN_{8-z}$ with the top of the 5*d* orbitals overlapping the Si-3*s*3*p* and N-2*p* orbitals. In addition, the introduction of Eu^{2+} leads to the reduction of the energy gap of $Si_{6-z}Al_zO_zN_{8-z}$.

(3) $Eu_xSi_{6-z}Al_{z-x}O_{z+x}N_{8-z-x}$ shows efficient green emission at about 530 nm when excited in the range of UV–405 nm. The position of the excitation and emission bands is almost independent of both Eu concentration (i.e., *x*) and type of dual-doping *M* (Li, Mg, Ca, Sr, and Ba). The emission band can only be shifted to long wavelength from 529 to 545 nm by an increase of *z* corresponding to a lattice expansion; as a result, the quantum efficiency is increased due to the increase in Eu–Eu and Eu–(Si/Al) distances. In addition, the emission intensity of Eu^{2+} can slightly be enhanced by co-doping Eu–Li and Eu–Ba without decreasing its thermal stability.

(4) The critical concentration of quenching of Eu^{2+} is very low at about $x=0.013$ in $Eu_xSi_{6-z}Al_{z-x}O_{z+x}N_{8-z-x}$, which is mainly attributed to photoionization, confirmed by both the experimental and first-principles calculations.

References

[1] J.W.H. van Krevel, J.W.T. van Rutten, H. Mandal, H.T. Hintzen, R. Metselaar, J. Solid State Chem. 165 (2002) 19.
[2] R.J. Xie, M. Mitomo, K. Uheda, F.F. Xu, Y. Akimune, J. Am. Ceram. Soc. 85 (2002) 1229.
[3] R.J. Xie, N. Hirosaki, K. Sakuma, Y. Yamamoto, M. Mitomo, Appl. Phys. Lett. 84 (2004) 5405.
[4] R.J. Xie, N. Hirosaki, M. Mitomo, Y. Yamamoto, T. Suehiro, K. Sakuma, J. Phys. Chem. B 108 (2004) 12027.
[5] T. Suehiro, N. Hirosaki, R.J. Xie, M. Mitomo, Chem. Mater. 17 (2005) 308.
[6] R.J. Xie, N. Hirosaki, M. Mitomo, K. Takahashi, K. Sakuma, Appl. Phys. Lett. 88 (2006) 101104.
[7] R.J. Xie, N. Hirosaki, M. Mitomo, K. Uheda, T. Suehiro, K. Sakuma, J. Phys. Chem. B 109 (2005) 9490.
[8] K.H. Jack, W.I. Wilson, Nat. Phys. Sci. (London) 238 (1972) 28.
[9] K.H. Jack, J. Mater. Sci. 11 (1976) 1135.
[10] T. Ekstrom, M. Nygren, J. Am. Ceram. Soc. 75 (1992) 259.
[11] G. Petzow, M. Herrmann, Struct. Bonding 102 (2002) 47.
[12] G.Z. Cao, R. Metselaar, Chem. Mater. 3 (1991) 242.
[13] K. Sakuma, K. Omichi, N. Kimura, M. Ohashi, D. Tanaka, N. Hirosaki, Y. Yamamoto, R.J. Xie, T. Suehiro, Opt. Lett. 29 (2004) 2001.
[14] K. Sakuma, N. Hirosaki, N. Kimura, M. Ohashi, R.J. Xie, Y. Yamamoto, T. Seuhiro, K. Asano, D. Tanaka, IEICE Trans. Electron. E 88-C (2005) 2057.
[15] T.J. Popma, European Patent, EP 0155047 A1, 1985.
[16] N. Hirosaki, X.J. Xie, K. Kimoto, T. Sekiguchi, Y. Yamamoto, T. Suehiro, M. Mitomo, Appl. Phys. Lett. 86 (2005) 211905.
[17] K. Uheda, N. Hirosaki, Y. Yamamoto, A. Naito, T. Nakajima, H. Yamamoto, Electrochem. Solid-State Lett. 9 (2006) 4.
[18] K. Uheda, N. Hirosaki, Y. Yamamoto, H. Yamamoto, Phys. Status Solidi (a) 203 (2006) 2712.
[19] N. Hirosaki, R.J. Xie, K. Sakuma, Bull. Ceram. Soc. Japan 41 (2006) 602.
[20] R.J. Xie, N. Hirosaki, H.L. Li, M. Mitomo, J. Electrochem. Soc. 154 (2007) J314.
[21] A.C. Larson, R.B. Von Dreele, Report LAUR 86-748, Los Alamos National Laboratory, Los Alamos, NM, 2000.
[22] B.H. Toby, J. Appl. Crystallogr. 34 (2001) 210.
[23] S. Wild, P. Grieveson, K.H. Jack, Spec. Ceram. 5 (1972) 385.
[24] A. Rośen, D.E. Ellis, H. Adachi, F.W. Averill, J. Chem. Phys. 65 (1976) 3629.
[25] H. Adachi, M. Tsukada, C. Satoko, Jpn. J. Phys. Soc. 45 (1978) 875.
[26] K. Ogasawara, T. Iwata, Y. Koyama, T. Ishii, I. Tanaka, H. Adachi, Phys. Rev. B 64 (2001) 115413.
[27] H. Yoshida, R. Yoshimatsu, S. Watanabe, K. Ogasawara, Jpn. J. Phys. Soc. 45 (2006) 146.
[28] T. Nakayasu, T. Yamada, I. Tanaka, H. Adachi, S. Goto, J. Am. Ceram. Soc. 80 (1997) 2525.
[29] T. Nakayasu, T. Yamada, I. Tanaka, H. Adachi, S. Goto, J. Am. Ceram. Soc. 81 (1998) 565.
[30] L. Gillott, N. Cowlam, G.E. Bacon, J. Mater. Sci. 16 (1981) 2263.
[31] F.K. van Dijen, R. Metselaar, R.B. Helmholdt, J. Mater. Sci. Lett. 6 (1987) 1101.
[32] H. Huppertz, W. Schnick, Acta Crystallogr. C 5319 (1997) 1751.
[33] R. Marchand, P. l'Haridon, Y. Laurent, J. Solid State Chem. 24 (1978) 71.
[34] B. Haferkorn, G. Meyer, Z. Anorg. Allg. Chem. 624 (1998) 1079.
[35] F. Stadler, O. Oeckler, H.A. Hoeppe, M.H. Moeller, R. Poettgen, B.D. Mosel, P. Schmidt, V. Duppel, A. Simon, W. Schnick, Chem. Eur. J. 12 (2006) 6719.
[36] Y.Q. Li, C.M. Fang, G. de With, H.T. Hintzen, J. Solid State Chem. 177 (2004) 4687.
[37] H. Jacobsen, G. Meyer, W. Schipper, G. Blasse, Z. Anorg. Allg. Chem. 620 (1994) 451.
[38] R. Hoppe, Angew. Chem. 78 (1966) 52.
[39] R. Hoppe, Angew. Chem. 82 (1970) 7.
[40] R. Hoppe, Adv. Fluoresc. Chem. 6 (1970) 387.
[41] M.B. Trigg, K.H. Jack, J. Mater. Sci. Lett. 6 (1987) 407.
[42] C.M. Fang, R. Metselaar, J. Mater. Chem. 13 (2003) 335.
[43] K. Tatsumi, I. Tankka, H. Adachi, M. Yoshiya, Phys. Rev. B 66 (2002) 165210.
[44] T. Schlieper, W. Milius, W. Schnick, Z. Anorg. Allg. Chem. 621 (1995) 1380.
[45] M. Catti, G. Gazzoni, G. Ivaldi, G. Zanini, Acta Crystallogr. B 39 (1983) 674.
[46] G. Blasse, B.C. Grabmaier, Luminescent Materials, Springer, Berlin, 1994.
[47] P. Dorenbos, J. Phys.: Condens. Matter 17 (2005) 8103.
[48] E. van der Kolk, P. Dorenbos, J.T.M. de Haas, C.W.E. van Eijk, Phys. Rev. B 71 (2005) 45121.
[49] K.P. O'Donnell, X. Chen, Appl. Phys. Lett. 58 (1991) 2924.
[50] Y.P. Varshni, Physica 34 (1967) 149.